Author/s:
Poon, EKW;Barlis, P;Moore, S;PAN, W;Liu, Y;YE, Y;XUE, Y;Zhu, SJ;Ooi, A

Title:
Numerical investigations of the haemodynamic changes associated with stent malapposition in an idealised coronary artery

Date:
2014

Citation:
Poon, E. K. W., Barlis, P., Moore, S., PAN, W., Liu, Y., YE, Y., XUE, Y., Zhu, S. J. & Ooi, A. (2014). Numerical investigations of the haemodynamic changes associated with stent malapposition in an idealised coronary artery. Journal of Biomechanics, 47 (12), pp.2843-2851. https://doi.org/10.1016/j.jbiomech.2014.07.030.

Persistent Link:
https://hdl.handle.net/11343/43840

www.elsevier.com/locate/jbiomech

Numerical investigations of the hemodynamic changes associated with stent malapposition in an idealised coronary artery

Eric K.W. Poon, Peter Barlis, Stephen Moore, Wei-Han Pan, Yun Liu, Yufei Ye, Yuan Xue, Shuang J. Zhu, Andrew S.H. Ooi

PII: S0021-9290(14)00421-7
DOI: http://dx.doi.org/10.1016/j.jbiomech.2014.07.030
Reference: BM6754

To appear in: *Journal of Biomechanics*

Received date: 28 January 2014
Revised date: 10 July 2014
Accepted date: 29 July 2014

Cite this article as: Eric K.W. Poon, Peter Barlis, Stephen Moore, Wei-Han Pan, Yun Liu, Yufei Ye, Yuan Xue, Shuang J. Zhu, Andrew S.H. Ooi, Numerical investigations of the hemodynamic changes associated with stent malapposition in an idealised coronary artery, *Journal of Biomechanics*, http://dx.doi.org/10.1016/j.jbiomech.2014.07.030

Original Article – There are in total 3500 words from Introduction through Discussion in this article.

Numerical investigations of the hemodynamic changes associated with stent malapposition in an idealised coronary artery

Eric K.W. Poon[a,*], Peter Barlis[a,b], Stephen Moore[c], Wei-Han Pan[a], Yun Liu[a], Yufei Ye[a], Yuan Xue[a], Shuang J. Zhu[a], Andrew S.H. Ooi[a]

[a] Department of Mechanical Engineering, Melbourne School of Engineering, The University Of Melbourne, Victoria 3010, Australia

[b] North West Academic Centre, Melbourne Medical School, The University of Melbourne, Victoria 3010, Australia

[c] IBM Research Collaboratory for Life Sciences-Melbourne, Victoria Life Sciences Computation Initiative, The University of Melbourne, Victoria 3010, Australia

Keywords: Stent malapposition, coronary stents, atherosclerosis, in-silico, wall shear stress

*Corresponding author: Tel.: +61 3 8344 3044; fax: +61 3 8344 4290.

E-mail address: epoon@unimelb.edu.au (E. Poon)

ABSTRACT

The deployment of a coronary stent near complex lesions can sometimes lead to incomplete stent apposition (ISA), an undesirable side effect of coronary stent implantation. 3-dimensional computational fluid dynamics (CFD) calculations are performed on simplified stent models (with either square or circular cross-section struts) inside an idealized coronary artery to analyse the effect of different levels of ISA to the change in hemodynamics inside the artery. The clinical significance of ISA is reported using hemodynamic metrics like wall shear stress (WSS) and wall shear stress gradient (WSSG). A coronary stent with square cross-sectional strut shows different levels of reverse flow for malapposition distance (MD) between 0mm and 0.12mm. Chaotic blood flow is usually observed at late diastole and early systole for MD = 0mm and 0.12mm but are suppressed for MD = 0.06mm. The struts with circular cross-section delay the flow chaotic process as compared to square cross-sectional struts at the same MD and also reduce the level of fluctuations found in the flow field. However, further increase in MD can lead to chaotic flow not only at late diastole and early systole, it also leads to chaotic flow at the end of systole. In all cases, WSS increases above the threshold value (0.5Pa) as MD increases due to the diminishing reverse flow near the artery wall. Increasing MD also results in an elevated WSSG as flow becomes more chaotic, except for square struts at MD = 0.06mm.

1. Introduction

The introduction of coronary stents with dual antiplatelet therapy has significantly improved the safety of percutaneous coronary intervention for treatment of coronary artery disease (Garg and Serruys, 2010a; Stefanini and Holmes, 2013). However, restenoses remained common with first generation bare metal stent (BMS) and thus led to the development of second-generation polymer coating drug-eluting stent (DES). Early trials of DES demonstrated outstanding results, but long-term safety of DES was questioned after studies showed higher rate of very late stent thrombosis (ST) (Martin and Boyle, 2011). Over

the years, advances in metallurgy and polymer technology have substantially improved the design of coronary stents (Garg and Serruys, 2010b). Although the use of stents has proven to be highly successful (Morlacchi and Migliavacca, 2013), incomplete stent apposition (ISA), detected using either intravascular ultrasound (Degertekin et al., 2003a, 2003b; Hoffmann et al., 2008; Hong et al., 2006; Serruys et al., 2002; van der Hoeven et al., 2008) or optical coherence tomography (Ferrante et al., 2013; Gonzalo et al., 2009; Santos et al., 2011), remains a challenge in complex lesions that has been linked with adverse clinical outcomes (Ako et al., 2005; Nakamura et al., 2003; Tanabe et al., 2005; Weissman et al., 2005). The linkage between ISA and ST/ISR is yet to be understood (Colombo and Latib, 2008). De Santis et al. (2013) suggested that ISA disturbs blood flow and results in a high shear force as one of the contributing factors to ST/ISR. Foin et al. (2014) also reported an increasing shear rate with large ISA. However, neither studies addressed the temporal and spatial distribution of shear force.

In recent years, computational fluid dynamics (CFD) has become a powerful research tool to provide insight into the hemodynamic changes in the proximity of a coronary stent. CFD can provide quantitative analysis on the negative effect on wall shear stress (WSS) and wall shear stress gradient (WSSG), that are associated with ST and ISR (Carlier et al., 2003; Ladisa et al., 2005c; Wentzel et al., 2008, 2001) and thus maybe used to optimise a stent design to limit regions of non-physiological flow (Balossino et al., 2008; Gundert et al., 2012a; Murphy and Boyle, 2010a). Despite the advancement of CFD in the hemodynamic performance of coronary stents from a relatively simple geometry (Balakrishnan et al., 2005; Duraiswamy et al., 2010; Gundert et al., 2012b; LaDisa et al., 2005b) to patient specific studies (Chiastra et al., 2013; Morlacchi et al., 2013; Rikhtegar et al., 2014), the approval of coronary stents is a long process that involves initial numerical and experimental tests and multiple tiers of clinical studies in animals and humans but not any initial assessment on the hemodynamic performance of coronary stents (Food and Drug Administration, 2013). An excellent review on the effects of different coronary stents in a simplified coronary artery was provided by Murphy and Boyle (2010b). They concluded that flow reattachment is essential

to maintain functional endothelial cells. Berry et al. (2000) and Frank et al. (2002) suggested a distance of 6 times greater than the strut thickness between adjacent struts for flow reattachment. However, this may come at the expense of increased platelet deposition (Frank et al., 2002) and an undesirable WSSG (LaDisa et al., 2005a).

In this study, we aim to improve our knowledge of the hemodynamic changes in the presence of a coronary stent. We focus on ISA and its clinical significance by systematically studying the level of ISA of a simplified coronary stent in an idealised coronary artery. This study will lead to a fundamental understanding of the level of ISA and the associated 3 dimensional hemodynamic changes in order to help model more complex vessel geometries and improve future coronary stent designs and deployment techniques.

2. Methodology

2.1. Computational fluid dynamics methods

The hemodynamics around a malapposed stent inside a coronary artery are numerically simulated using CFD. Blood is assumed to be Newtonian with a constant density of 1,000kg/m^3 and kinematic viscosity of 2.5×10^{-3}Pa·s (Gousios and Shearn, 1959). The artery wall is assumed to be rigid and blood flow inside is computed by directly solving the incompressible Navier—Stokes equations using a finite-volume solver OpenFOAM (OpenCFD Ltd.) with the convective term approximated by Gauss linear corrected scheme; Gauss self-filter central differencing scheme and Crank-Nicolson scheme for diffusive and unsteady terms, respectively. Relaxation factors for pressure and velocity are 0.5 and 0.7, respectively. Pressure and velocity coupling are through a standard PISO algorithm with a time step size of ~0.0014s (640 time steps per cardiac cycle). Convergence criteria for both pressure and velocity residuals are 10^{-5} for accurate solutions (Balossino et al., 2008). A time-dependent velocity profile (Womersley, 1955) is prescribed at the inlet to mimic pulsatile blood flow behaviour. The physiological waveform is obtained from Sherwin and Blackburn

(2005). Both the artery wall and coronary stent are considered no-slip, and a zero pressure is employed at the outlet boundary.

2.2. Idealised coronary artery and simplified stent models

Fig. 1 presents a schematic diagram of the idealised coronary artery, simplified stent models and the chosen physiological waveform. The coronary artery is assumed to be a cylindrical tube with a constant diameter of 3mm (Bhimalli et al., 2011; Dodge et al., 1992; Ilayperuma et al., 2011; Spiller et al., 1983). In this study, the coronary stent is simplified as either square or circular cross-sections rings (red colour). Similar simplified stent models have been utilised by Jiménez and Davies (2009) to study the hemodynamic changes of different strut shapes. The stent struts have a thickness of T = 0.12mm. A total of 10 rings with ring-to-ring distance of L = 4.2mm is considered. The geometry and computational mesh were generated by ICEM-CFD (ANSYS INC., Canonsburg, PA, USA), which has approximately 7 million hexahedral cells. A grid resolution study was also performed by doubling the number of hexahedral cells and found no significant difference in the important hemodynamic metrics.

The pulsatile waveform is shown at the bottom left of Fig. 1. The first peak of the waveform represents diastole followed by systole at the second peak. We simulated a patient undergoing light to moderate exercise with a diastolic blood velocity of 3.61m/s, which is approximately 5 times the resting blood flow velocity reported by Nagel et al. (2003) and Ofili et al. (1993). i.e., a coronary flow reserve approximately equal to 5 (Gould et al., 2013; Schwartzkopff et al., 1998). The mean blood flow velocity is 1.44m/s which corresponds to a mean blood flow rate of 600mL/min (Thibodeau and Patton, 2007). We considered the heart beat to be 70beats/min.

2.3. Hemodynamic metrics

In order to understand the effects of hemodynamic changes as a result of ISA, two of the most important hemodynamic metrics, WSS and WSSG, are employed. The WSS and WSSG are shown to have significant correlations with excessive neointimal hyperplasia (NH), which is the main reason for ISR (Buchanan et al., 2003, 2000; Hyun et al., 2001; Murphy and Boyle,

2007). Low WSS (< 0.5Pa) affects the shape and alignment of the endothelial cells that increase the permeability of the endothelial layer and thus excessive NH (Malek et al., 1999). On the other hand, endothelial cells that act as a barrier to NH grows are pushed away from high WSSG regions (>5,000Pa/m) (DePaola et al., 1992).

3. Results

CFD studies are carried out for four cardiac cycles (CC). The chaotic flow field around a stent is revealed by plotting the time evolution of WSS at the fourth CC. Statistical behaviour of WSS and WSSG are time-averaged over the fourth CC and report as TWSS and TWSSG. Fig. 2 presents the WSS contours of the simplified square struts attached to the idealized coronary artery. As the flow field is 3-dimenisonal and changes along the azimuthal direction (ϕ), the artery wall is artificially cut open and unwrapped into a 2-dimensional plane (Z *versus* ϕ) to clearly demonstrate 3-dimenional nature of the flow field.

3.1. Effect of malapposition distance

Figs. 3, 4 and 5 present the WSS contours over a CC for square struts at MD = 0mm, 0.06mm and 0.12mm, respectively. When the struts are attached to the wall (MD = 0mm), WSS decreases sharply and becomes negative distal to the square struts throughout the acceleration stage of diastole and initial deceleration stage of diastole from point (a) to (c). The WSS contours increase slowly and become positive again proximal to the subsequent strut. The WSS contours maintain a constant value along the ϕ-direction. The negative WSS contours indicate reverse flow distal to the struts as the presence of the attached struts resembles the flow past backward-facing steps (Biswas et al., 2004). The flow is reattached behind these reverse flow regions and WSS returns positive. This is consistent with Berry et al. (2000) and Frank et al. (2002) who stated that flow attachment is observed for strut distances > 6*T*. Chaotic WSS patterns are observed from the end of diastole (d) to early systole (f). In (d) WSS is highly irregular after the sixth strut. The WSS patterns remain chaotic in (e), but the variation in WSS magnitude decreases significantly. In (f), irregularity of WSS is only

observed distal to the eighth strut. In other words, the fluctuations in the flow field decreases in (e) and (f). During systole ((g) to (h)), the WSS is constant along the ϕ-direction indicating laminar blood flow.

For MD = 0.06mm, the WSS contours are constant along the ϕ-direction through (a) to (d). Negative WSS in (b) and (d) are detached from the square struts. This is because reverse flow distal to a malapposed strut is governed by a different mechanism: the roll-up of vorticity in between the struts and the artery wall (Lei et al., 2006; Price et al., 2002; Wang and Tan, 2008). The WSS patterns show signs of irregularity distal to the tenth strut in (e) but this irregularity subsides for the remainder of the CC. i.e., chaotic flow is suppressed for MD = 0.06mm.

For MD = 0.12mm, WSS values are positive through (a) to (b) and irregular WSS patterns are observed distal the seventh strut as early as (b). The WSS is highly chaotic throughout (c) to (e). WSS becomes irregular distal the fifth strut in (c). This irregularity travels downstream and only appears after seventh strut in (d) and eighth strut in (e). WSS is constant along the ϕ-direction for the remainder of the CC. The positive WSS value in (a) shows that there is no longer any reverse flow at this MD. This is because the square struts are considered to be isolated from the artery wall (Price et al., 2002). As a result, the blood flow behind the struts interacts less with the boundary layer from the artery wall. However, the struts are subjected to higher blood flow velocity near the centre of the artery (see velocity profile at the bottom right of Fig. 1). The higher local velocity leads to earlier onset of flow instability and longer period of chaotic flow. Chaotic blood flow is also observed proximal to the sixth strut for MD = 0.12mm.

3.2. Square struts versus circular struts

Fig. 6 presents the WSS patterns for circular struts at MD = 0.12mm. The WSS are positive and constant along the ϕ-direction through (a) to (b). It becomes irregular in (c); highly chaotic in (d) and irregularities subside in (e). However, unlike square struts at MD = 0.12mm (see Fig. 5), these irregular WSS patterns are confined to the last three struts. The WSS

remains positive and constant along the ϕ-direction for the rest of the CC. The deployment of circular struts has dramatically reduced flow fluctuations. This is because the flow past a circular cylinder is known to have a later onset of flow instability. In fact, the flow instability begins at $Re = O(10)$ for square (Gera et al., 2010) but $Re = O(100)$ for cylinder (Smits, 2000).

3.3. Large malapposition distance

The effect of large MD on the hemodynamics is also investigated and WSS patterns for circular struts at MD = 0.24mm are shown in Fig. 7. From (a) to (b), the WSS is positive and constant along the ϕ-direction. Chaotic WSS patterns begin in (c) just proximal to the eighth strut. The variations in WSS are more pronounced at MD = 0.24mm as struts are closer to the centre of the artery and thus are subjected to a higher blood flow velocity. WSS becomes highly chaotic in (d) distal to the fifth strut. The variation in WSS decreases in (e) and is only observed distal to the seventh strut. The WSS becomes constant along the ϕ-direction until (h) when chaotic WSS patterns are once again observed in the vicinity of the tenth strut.

3.4. Time averaged WSS and WSSG

The long-term hemodynamic behavior for ISA is studied using TWSS and TWSSG as presented in Fig. 8. Square struts always lead to TWSS < 0.5Pa regardless of MD. On the other hand, the deployment of circular struts only shows low TWSS for MD = 0.12mm proximal to the tenth strut. The low TWSS for the square struts is attributed to the reverse flows behind the struts. In fact, square struts at MD = 0mm act as backward-facing steps that lead to strong reverse flows and lowest TWSS. As MD increases, reverse flows are less strong and TWSS increases gradually until MD = 0.12mm, where TWSS above 60Pa (similar to the TWSS reported by De Santis et al., 2013) is observed from the first to the eighth strut. The low TWSS distal to the eighth strut maybe attributed to the chaotic flow.

The deployment of square and circular stent struts at different levels of ISA also affects the TWSSG. For attached square struts, because of the reverse flows and flow reattachments, they show the highest TWSSG in between the first seven struts. Increasing MD leads to low

TWSSG in between the first seven struts. After the seventh strut, TWSSG is substantially higher at MD = 0mm and 0.12mm as flow is chaotic. However, for square struts at MD = 0.06mm, chaotic flow is suppressed and thus TWSSG is below the threshold (5,000Pa/m). For circular struts at MD = 0.12mm, flow is less chaotic as compared to square struts at the same MD. Therefore, TWSSG < 5,000Pa/m proximal to the eighth strut. Further increase in MD results in high TWSSG (>5,000Pa/m) distal to the sixth strut.

Fig. 9 presents the lumen area affected by low TWSS or high TWSSG over the stented area. Despite the decrease in TWSS for square struts with increasing MD. The lumen area affected by low TWSS increases initially for MD = 0.06mm before it decreases at MD = 0.12mm. For square struts at MD = 0.06mm, more than 50% of the lumen area is affected by TWSS < 0.5Pa as a result of elongated reverse flow regions. The chaotic flow at MD = 0.12mm increases the lumen area affected by low TWSS. The use of circular struts minimises chaotic flow and significantly reduces the affected area. At MD = 0.24mm, the circular struts do not result in any low TWSS area.

The lumen area affected by high TWSSG is the highest for square struts at MD = 0.00mm followed by MD = 0.12. MD = 0.06mm shows the smallest affected area as the chaotic flow is suppressed. Circular struts have a smaller affected area at MD = 0.12mm as compared to square struts but increases with large MD. In general, chaotic flow increases the area affected by high TWSSG.

4. Discussion

The effect of ISA on the hemodynamic changes in a coronary artery is studied systematically using CFD. The coronary stent is simplified into either square/circular strut rings inside an idealised coronary artery. The employment of such a simplified model allows for a better understanding of different levels of ISA and their clinical significance on ST/ISR by studying WSS and WSSG and provides the foundation of further studies of more complex stent and vessel geometries.

The presence of square struts attached to the artery wall (MD = 0mm) leads to reverse flow similar to the flow past backward-facing steps (Biswas et al., 2004). As a result, low/negative WSS is calculated (see Fig. 8) and a large lumen area covered by low TWSS (Fig. 9). However, long separation between adjacent struts results in flow reattachment. Both rapid changes in flow direction and chaotic flow lead to a high WSSG. This configuration also results in the largest coverage of TWSSG above threshold (> 5,000Pa/m) on the lumen surface. At MD = 0.06mm, reverse flows governed by the interaction between the wall boundary layer and the presence of the square struts (Lei et al., 2006; Price et al., 2002; Wang and Tan, 2008) are observed, but are less strong. Longer reverse flow regions cause an increase in lumen area with low TWSS. Chaotic flow is supressed for this MD that reduces the lumen area with TWSSG > 5,000Pa/m. Further increase in MD leads to an elongated period of chaotic flow. The highly chaotic blood flow results in high WSSG (affected lumen area increases to 23% at MD = 0.12mm as shown in Fig. 9). However, as MD increases, there is less interaction between the wall boundary layer and the flow past the square struts. As a result, reverse flow is diminished and WSS is almost always higher than the threshold along the artery (lumen area with TWSS < 0.5Pa decreases to 14%).

Replacing the square struts with circular struts delays the occurrence of chaotic flow due to later onset of flow instability for circular cylinder. The chaotic blood flow also occurs further downstream (distal to the eighth circular strut as shown in Fig. 6 as compared to the fifth square strut in Fig. 5). This results in a significantly lower WSSG distal to the fifth circular strut and a smaller lumen area (11%) above the TWSSG threshold. A further increase MD (0.24mm) enhances chaotic flow. Chaotic flow is observed just distal to the fifth strut which increases the affected lumen area (from 11% to 33% as reported in Fig. 9). However, both absolute maximum TWSS and TWSSG remain lower than square struts at MD = 0.12mm (Fig. 8). Lumen area with TWSS < 0.5Pa is almost insignificant for circular struts.

4.1. Limitations and further studies

In this in-silico study, it is interesting to note that deployment of square struts at MD = 0.06mm led to suppression of chaotic flow. It also outlines several other contradicting results such as an increase in both WSS and WSSG above the threshold with increasing MD, one of which leads to ST/ISR (high WSSG) while the other gives a false secure reading (high WSS). However, due to the idealised geometry of the stent, this study can only provide an initial preliminary (and general) assessment on how the WSS and WSSG are affected by various degrees of ISA. The results in this study should thus be interpreted with care.

Furthermore, the idealised coronary artery disregards any curvature and stenosis. This can have a direct consequence on both WSS and WSSG as any secondary flow and radial forces are not considered. The distensibility of the artery wall and the effect of intramyocardiac pressure are also neglected. In some sense, some of these assumptions are justified as stent deployment has been shown to straighten and reduce the compliance of the artery wall (Balossino et al., 2008). In addition, the intramyocardiac pressure may affect the instantaneous WSS but not TWSS (Chiastra et al., 2013). On the other hand, simplification of a coronary stent to either square or circular strut rings will have a more pronounced effect on the hemodynamics. The fluid interactions with the stent cross members and the artery wall may introduce more fluctuations into the flow field and change both WSS and WSSG substantially. However, the employment of a commercially available stent to study the effect of ISA may require extensive computational power and storage. Therefore, a simplified model was proposed in this study to identify the MD that would lead to hemodynamic metrics for the “worst case scenario”. This information will be utilised in future CFD studies with the deployment of an accurate representation of commercially available stent in either a circular coronary artery or patient specific artery.

Blood acts as a Newtonian fluid for shear rate above 100/s and is assumed to be Newtonian in the present study as Foin et al. (2014) demonstrated that ISA leads to shear rate above threshold. Due to the difficulties and limitations in in-vivo blood velocity measurement (Chiastra et al., 2013), blood flow velocity for an exercising patient is considered to be

approximately 4-5 times the resting blood flow velocity measured by Nagel et al. (2003) and Ofili et al. (1993). i.e., with CFR ~ 4-5 (Gould et al., 2013; Schwartzkopff et al., 1998). Lastly, zero pressure outlet may induce unrealistic physiological transient pressure, but is offset by the prescribed Dirichlet velocity boundary condition (Murphy and Boyle, 2010b) and lengthen outlet boundary from the strut rings (Carlier et al., 2003).

Conflict of interest statement

The authors Eric K. W. Poon, Peter Barlis, Stephen Moore, Wei-Han Pan, Yun Liu, Yufei Ye, Yuan Xue, Shuang J. Zhu and Andrew S. H. Ooi hereby declare that they have no conflict of interest.

Acknowledgements

The authors would like to acknowledge the support of the Australian Research Council for this research through ARC Linkage Project LP120100233. This research was also supported by a Victorian Life Sciences Computation Initiative (VLSCI) grant number (VR0210) on its Peak Computing Facility at the University of Melbourne, an initiative of the Victorian Government, Australia.

Reference

Ako, J., Morino, Y., Honda, Y., Hassan, A., Sonoda, S., Yock, P.G., Leon, M.B., Moses, J.W., Bonneau, H.N., Fitzgerald, P.J., 2005. Late incomplete stent apposition after sirolimus-eluting stent implantation: A serial intravascular ultrasound analysis. J. Am. Coll. Cardiol. 46, 1002–1005.

Balakrishnan, B., Tzafriri, A.R., Seifert, P., Groothuis, A., Rogers, C., Edelman, E.R., 2005. Strut position, blood flow, and drug deposition: implications for single and overlapping drug-eluting stents. Circulation 111, 2958–2965.

Balossino, R., Gervaso, F., Migliavacca, F., Dubini, G., 2008. Effects of different stent designs on local hemodynamics in stented arteries. J. Biomech. 41, 1053–61.

Berry, J., Santamarina, A., Moore, JamesE., J., Roychowdhury, S., Routh, W., 2000. Experimental and computational flow evaluation of coronary stents. Ann. Biomed. Eng. 28, 386–398.

Bhimalli, S., Dixit, D., Siddibhavi, M., Shirol, V.S., 2011. A study of variations in coronary arterial system in cadaveric human heart. World J. Sci. Tech. 1, 30–35.

Biswas, G., Breuer, M., Durst, F., 2004. Backward-facing step flows for various expansion ratios at low and moderate Reynolds numbers. J. Fluids Eng. 126, 362–374.

Buchanan, J.R., Kleinstreuer, C., Comer, J.K., 2000. Rheological effects on pulsatile hemodynamics in a stenosed tube. Comput. Fluids 29, 695–724.

Buchanan, J.R., Kleinstreuer, C., Hyun, S., Truskey, G. a., 2003. Hemodynamics simulation and identification of susceptible sites of atherosclerotic lesion formation in a model abdominal aorta. J. Biomech. 36, 1185–1196.

Carlier, S.G., van Damme, L.C. a, Blommerde, C.P., Wentzel, J.J., van Langehove, G., Verheye, S., Kockx, M.M., Knaapen, M.W.M., Cheng, C., Gijsen, F., Duncker, D.J., Stergiopulos, N., Slager, C.J., Serruys, P.W., Krams, R., 2003. Augmentation of wall shear stress inhibits neointimal hyperplasia after stent implantation: inhibition through reduction of inflammation? Circulation 107, 2741–6.

Chiastra, C., Morlacchi, S., Gallo, D., Morbiducci, U., Cárdenes, R., Larrabide, I., Migliavacca, F., 2013. Computational fluid dynamic simulations of image-based stented coronary bifurcation models. J. R. Soc. Interface 10, 20130193.

Colombo, A., Latib, A., 2008. Late incomplete stent apposition after drug-eluting stent implantation: a true risk factor or “an innocent bystander”? Heart 94, 253–4.

De Santis, G., Trachet, B., Conti, M., De Beule, M., Morbiducci, U., Mortier, P., Segers, P., Verdonck, P., Verhegghe, B., 2013. A computational study of the hemodynamic impact of open- versus closed-cell stent design in carotid artery stenting. Artif. Organs 37, E96–106.

Degertekin, M., Regar, E., Tanabe, K., Lemos, P., Lee, C.H., Smits, P., de Feyter, P., Bruining, N., Sousa, E., Abizaid, A., Ligthart, J., Serruys, P.W., 2003a. Evaluation of coronary remodeling after Sirolimus-Eluting stent implantation by serial Three-Dimensional intravascular ultrasound. Am. J. Cardiol. 91, 1046–1050.

Degertekin, M., Serruys, P.W., Tanabe, K., Lee, C.H., Sousa, J.E., Colombo, A., Morice, M.-C., Ligthart, J.M.R., de Feyter, P.J., 2003b. Long-term follow-up of incomplete stent apposition in patients who received sirolimus-eluting stent for de novo coronary lesions: an intravascular ultrasound analysis. Circulation 108, 2747–50.

DePaola, N., Gimbrone, M. a., Davies, P.F., Dewey, C.F., 1992. Vascular endothelium responds to fluid shear stress gradients. Arter. Throm. Vas. 12, 1254–1257.

Dodge, J.T., Brown, B.G., Bolson, E.L., Dodge, H.T., 1992. Lumen diameter of normal human coronary arteries. Influence of age, sex, anatomic variation, and left ventricular hypertrophy or dilation. Circulation 86, 232–246.

Duraiswamy, N., Schoephoerster, R.T., Moore, J.E., 2010. Comparison of near-wall hemodynamic parameters in stented artery models. J. Biomech. Eng. 131, 061006.

Ferrante, G., Presbitero, P., Whitbourn, R., Barlis, P., 2013. Current applications of optical coherence tomography for coronary intervention. Int. J. Cardiol. 165, 7–16.

Foin, N., Gutiérrez-Chico, J.L., Nakatani, S., Torii, R., Bourantas, C. V, Sen, S., Nijjer, S., Petraco, R., Kousera, C., Ghione, M., Onuma, Y., Garcia-Garcia, H.M., Francis, D.P., Wong, P., Di Mario, C., Davies, J.E., Serruys, P.W., 2014. Incomplete stent apposition causes high shear flow disturbances and delay in neointimal coverage as a function of strut to wall detachment distance: implications for the management of incomplete stent apposition. Circ. Cardiovasc. Interv. 7, 180–9.

Food and Drug Administration, 2013. Guidance for industry and FDA staff - Non-clinical engineering tests and recommended labeling for intravascular stents and associated delivery systems. Rockville, MD: U.S.

Frank, A.O., Walsh, P.W., Moore, J.E., 2002. Computational fluid dynamics and stent design. Artif. Organs 26, 614–621.

Garg, S., Serruys, P.W., 2010a. Coronary stents: current status. J. Am. Coll. Cardiol. 56, S1–42.

Garg, S., Serruys, P.W., 2010b. Coronary stents: looking forward. J. Am. Coll. Cardiol. 56, S43–78.

Gera, B., Sharma, P.K., Singh, R.K., 2010. CFD analysis of 2D unsteady flow around a square cylinder. Int. J. Appl. Eng. Res. 1, 602–610.

Gonzalo, N., Barlis, P., Serruys, P.W., Garcia-Garcia, H.M., Onuma, Y., Ligthart, J., Regar, E., 2009. Incomplete stent apposition and delayed tissue coverage are more frequent in drug-eluting stents implanted during primary percutaneous coronary intervention for ST-segment elevation myocardial infarction than in drug-eluting stents implanted for stable/un. JACC. Cardiovasc. Interv. 2, 445–52.

Gould, K.L., Johnson, N.P., Bateman, T.M., Beanlands, R.S., Bengel, F.M., Bober, R., Camici, P.G., Cerqueira, M.D., Chow, B.J.W., Di Carli, M.F., Dorbala, S., Gewirtz, H., Gropler, R.J., Kaufmann, P. a, Knaapen, P., Knuuti, J., Merhige, M.E., Rentrop, K.P., Ruddy, T.D., Schelbert, H.R., Schindler, T.H., Schwaiger,

M., Sdringola, S., Vitarello, J., Williams, K. a, Gordon, D., Dilsizian, V., Narula, J., 2013. Anatomic versus physiologic assessment of coronary artery disease. Role of coronary flow reserve, fractional flow reserve, and positron emission tomography imaging in revascularization decision-making. J. Am. Coll. Cardiol. 62, 1639–53.

Gousios, a., Shearn, M. a., 1959. Effect of Intravenous Heparin on Human Blood Viscosity. Circulation 20, 1063–1066.

Gundert, T.J., Marsden, A.L., Yang, W., LaDisa, J.F., 2012a. Optimization of cardiovascular stent design using computational fluid dynamics. J. Biomech. Eng. 134, 011002.

Gundert, T.J., Marsden, A.L., Yang, W., Marks, D.S., LaDisa, J.F., 2012b. Identification of hemodynamically optimal coronary stent designs based on vessel caliber. IEEE Trans. Biomed. Eng. 59, 1992–2002.

Hoffmann, R., Morice, M.-C., Moses, J.W., Fitzgerald, P.J., Mauri, L., Breithardt, G., Schofer, J., Serruys, P.W., Stoll, H.-P., Leon, M.B., 2008. Impact of late incomplete stent apposition after sirolimus-eluting stent implantation on 4-year clinical events: intravascular ultrasound analysis from the multicentre, randomised, RAVEL, E-SIRIUS and SIRIUS trials. Heart 94, 322–8.

Hong, M.-K., Mintz, G.S., Lee, C.W., Park, D.-W., Park, K.-M., Lee, B.-K., Kim, Y.-H., Song, J.-M., Han, K.-H., Kang, D.-H., Cheong, S.-S., Song, J.-K., Kim, J.-J., Park, S.-W., Park, S.-J., 2006. Late stent malapposition after drug-eluting stent implantation: an intravascular ultrasound analysis with long-term follow-up. Circulation 113, 414–9.

Hyun, S., Kleinstreuer, C., Archie, J.P., 2001. Computational particle-hemodynamics analysis and geometric reconstruction after carotid endarterectomy. Comput. Biol. Med. 31, 365–84.

Ilayperuma, I., Nanayakkara, B.G., Palahepitiya, K.N., 2011. Sexual differences in the diameter of coronary arteries in an adult Sri Lankan population. Int. J. Morphol. 29, 1444–1448.

Jiménez, J.M., Davies, P.F., 2009. Hemodynamically driven stent strut design. Ann. Biomed. Eng. 37, 1483–94.

LaDisa, J.F., Olson, L.E., Guler, I., Hettrick, D.A., Kersten, J.R., Warltier, D.C., Pagel, P.S., 2005a. Circumferential vascular deformation after stent implantation alters wall shear stress evaluated with time-dependent 3D computational fluid dynamics models 98, 947–957.

LaDisa, J.F., Olson, L.E., Hettrick, D. a, Warltier, D.C., Kersten, J.R., Pagel, P.S., 2005b. Axial stent strut angle influences wall shear stress after stent implantation: analysis using 3D computational fluid dynamics models of stent foreshortening. Biomed. Eng. Online 4, 59.

Ladisa, J.F., Olson, L.E., Molthen, R.C., Hettrick, D.A., Pratt, P.F., Hardel, M.D., Kersten, J.R., Warltier, D.C., Pagel, P.S., John, F., Hettrick, A., 2005. Alterations in wall shear stress predict sites of neointimal hyperplasia after stent implantation in rabbit iliac arteries 53226, 2465–2475.

Lei, C., Cheng, L., Armfield, S.W., Kavanagh, K., 2006. Vortex shedding suppression for flow over a circular cylinder near a plane boundary. Ocean Eng. 27, 1109–1127.

Malek, A.M., Alper, S.L., Izumo, S., 1999. Hemodynamic shear stress and its role in atherosclerosis. J. Am. Med. Assoc. 282, 2035–2042.

Martin, D.M., Boyle, F.J., 2011. Drug-eluting stents for coronary artery disease: a review. Med. Eng. Phys. 33, 148–63.

Morlacchi, S., Colleoni, S.G., Cárdenes, R., Chiastra, C., Diez, J.L., Larrabide, I., Migliavacca, F., 2013. Patient-specific simulations of stenting procedures in coronary bifurcations: two clinical cases. Med. Eng. Phys. 35, 1272–81.

Morlacchi, S., Migliavacca, F., 2013. Modeling stented coronary arteries: where we are, where to go. Ann. Biomed. Eng. 41, 1428–44.

Murphy, J., Boyle, F., 2007. Comparison of stent designs using computational fluid fynamics, in: 10th Annual Sir Berbard Crossland Symposium. Dublin.

Murphy, J., Boyle, F., 2010a. A numerical methodology to fully elucidate the altered wall shear stress in a stented coronary artery. Cardiovasc. Eng. Tech. 1, 256–268.

Murphy, J., Boyle, F., 2010b. Predicting neointimal hyperplasia in stented arteries using time-dependant computational fluid dynamics: a review. Comput. Biol. Med. 40, 408–18.

Nagel, E., Thouet, T., Klein, C., Schalla, S., Bornstedt, A., Schnackenburg, B., Hug, J., Wellnhofer, E., Fleck, E., 2003. Noninvasive determination of coronary blood flow velocity with cardiovascular magnetic resonance in patients after stent deployment. Circulation 107, 1738–43.

Nakamura, M., Kataoka, T., Honda, Y., Bonneau, H.N., Hibi, K., Kitamura, K., Tamai, H., Aizawa, T., Yock, P.G., Fitzgerald, P.J., 2003. Late incomplete stent apposition and focal vessel expansion after bare metal stenting. Am. J. Cardiol. 92, 1217–1219.

Ofili, E.O., Kern, M.J., Labovitz, A.J., Vrain, J.A.S., Segal, J., Aguirre, F. V, Castello, R., 1993. Analysis of coronary blood flow velocity dynamics in angiographically normal and stenosed arteries before and after endolumen enlargement by angioplasty. J. Am. Coll. Cardiol. 21, 308–316.

OpenCFD Ltd., n.d. No Title [WWW Document]. URL http://openfoam.com/

Price, S.J., Summer, D., Smith, J.G., Leong, K., Paidoussis, M.P., 2002. Flow visualization around a circular cylinder near to a plane wall. J. Fluids Struct. 16, 175–191.

Rikhtegar, F., Wyss, C., Stok, K.S., Poulikakos, D., Müller, R., Kurtcuoglu, V., 2014. Hemodynamics in coronary arteries with overlapping stents. J. Biomech. 47, 505–11.

Santos, M.C., Lin, T., Barlis, P., 2011. In-stent restenosis associated with stent malapposition: Seven year optical coherence tomography findings. Int. J. Cardiol. 147, 149–151.

Schwartzkopff, B., Mundhenke, M., Strauer, B.E., 1998. Alterations of the architecture of subendocardial arterioles in patients with hypertrophic cardiomyopathy and impaired coronary vasodilator reserve: a possible cause for myocardial ischemia. J. Am. Coll. Cardiol. 31, 1089–96.

Serruys, P.W., Degertekin, M., Tanabe, K., Abizaid, A., Sousa, J.E., Colombo, A., Guagliumi, G., Wijns, W., Lindeboom, W.K., Ligthart, J., de Feyter, P.J., Morice, M.-C., 2002. Intravascular ultrasound findings in the multicenter, randomized, double-blind RAVEL (RAndomized study with the sirolimus-eluting VElocity balloon-expandable stent in the treatment of patients with de novo native coronary artery Lesions) Trial. Circulation 106, 798–803.

Sherwin, S.J., Blackburn, H.M., 2005. Three-dimensional instabilities and transition of steady and pulsatile axisymmetric stenotic flows. J. Fluid Mech. 533, 297–327.

Smits, A.J., 2000. Drag of bluff body and streamlined bodies, in: A Physical Introduction to Fluid Mechanics. John Wiley & Sons, Inc., New York, pp. 298–329.

Spiller, P., Schmiel, F.K., Politz, B., Block, M., Fermor, U., Hackbarth, W., Jehle, J., Korfer, R., Pannek, H., 1983. Measurement of systolic and diastolic flow rates in the coronary artery system by X-ray densitometry. Circulation 68, 337–347.

Stefanini, G.G., Holmes, D.R., 2013. Drug-eluting coronary-artery stents. New Engl. J. Med. 368, 254–65.

Tanabe, K., Serruys, P.W., Degertekin, M., Grube, E., Guagliumi, G., Urbaszek, W., Bonnier, J., Lablanche, J.-M., Siminiak, T., Nordrehaug, J., Figulla, H., Drzewiecki, J., Banning, A., Hauptmann, K., Dudek, D., Bruining, N., Hamers, R., Hoye, A., Ligthart, J.M.R., Disco, C., Koglin, J., Russell, M.E., Colombo, A., 2005. Incomplete stent apposition after implantation of paclitaxel-eluting stents or bare metal stents: insights from the randomized TAXUS II trial. Circulation 111, 900–5.

Thibodeau, G.A., Patton, K.T., 2007. Anatomy & Physiology, 6th ed, Anatomy & physiology. Mosby Elsevier, St. Louis, Missouri.

Van der Hoeven, B.L., Liem, S.-S., Jukema, J.W., Suraphakdee, N., Putter, H., Dijkstra, J., Atsma, D.E., Bootsma, M., Zeppenfeld, K., Oemrawsingh, P. V, van der Wall, E.E., Schalij, M.J., 2008. Sirolimus-eluting stents versus bare-metal stents in patients with ST-segment elevation Myocardial infarction: 9-month angiographic and intravascular ultrasound results and 12-month clinical outcome: results from the MISSION! Intervention study. J. Am. Coll. Cardiol. 51, 618–626.

Wang, X.K., Tan, S.K., 2008. Near-wake flow characteristics of a circular cylinder close to a wall. J. Fluids Struct. 24, 605–627.

Weissman, N.J., Koglin, J., Cox, D.A., Hermiller, J., O'Shaughnessy, C., Mann, J.T., Turco, M., Caputo, R., Bergin, P., Greenberg, J., Kutcher, M., Wong, S.C., Strickland, W., Mooney, M., Russell, M.E., Ellis, S.G., Stone, G.W., 2005. Polymer-based paclitaxel-eluting stents reduce in-stent neointimal tissue proliferation: A serial volumetric intravascular ultrasound analysis from the TAXUS-IV trial. J. Am. Coll. Cardiol. 45, 1201–1205.

Wentzel, J.J., Gijsen, F.J.H., Schuurbiers, J.C.H., van der Steen, A., Serruys, P.W., 2008. The influence of shear stress on in-stent restenosis and thrombosis. EuroIntervention 4, C27–C23.

Wentzel, J.J., Krams, R., Schuurbiers, J.C.H., Oomen, J. a., Kloet, J., van der Giessen, W.J., Serruys, P.W., Slager, C.J., 2001. Relationship between neointimal thickness and shear stress after Wallstent implantation in human coronary arteries. Circulation 103, 1740–1745.

Womersley, J.R., 1955. Method for the calculation of velocity, rate of flow and viscous drag in arteries when the pressure gradient is known. J. Physiol. 127, 553–563.

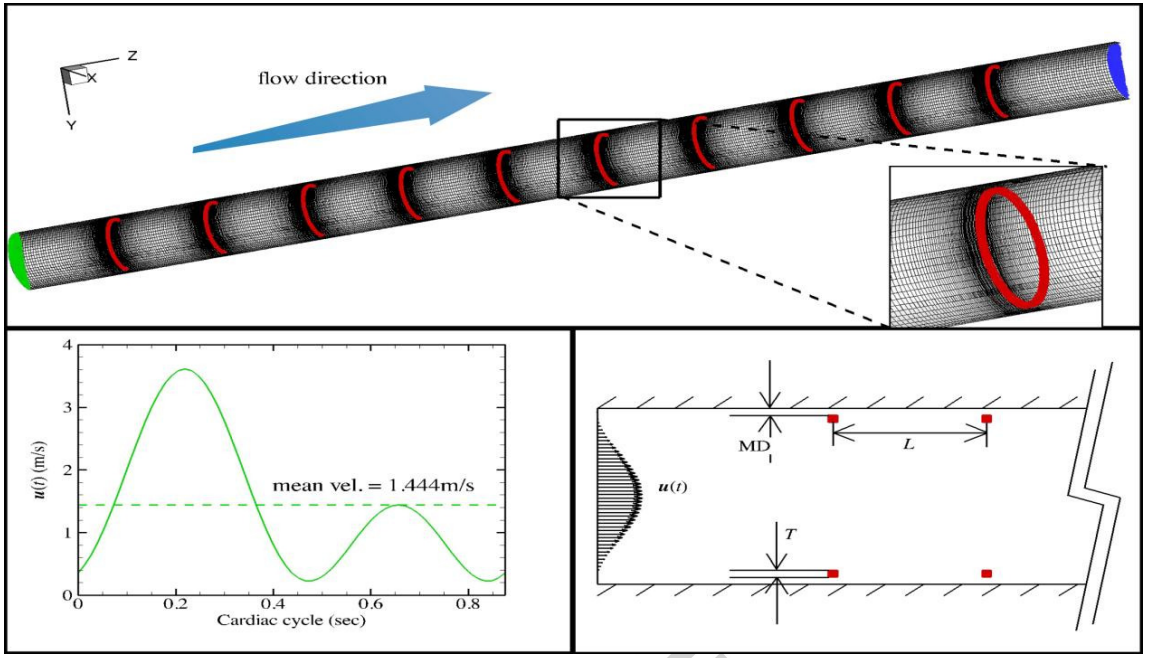

Fig. 1. (Top) schematic diagram of a simplified coronary stent inside an idealised coronary artery. The diagram only shows the computational domain in -ve *x*-direction. The black surface represents the coronary artery wall, red rings are the simplified coronary struts, green surface represents the proximal end of the artery and blue surface is the distal end of the artery. Inset demonstrates the grid sketching near the stent strut (red ring). (Bottom left) the pulsatile waveform, the first hill represents the diastole follows by systole in the second hill. (Bottom right) the pulsatile waveform is applied to the inlet of the computational domain (left hand end of the diagram). The malapposition distances, MD, are varied between 0 to 0.24mm and the distance between two consecutive struts (rings) is fixed at L = 4.2mm.

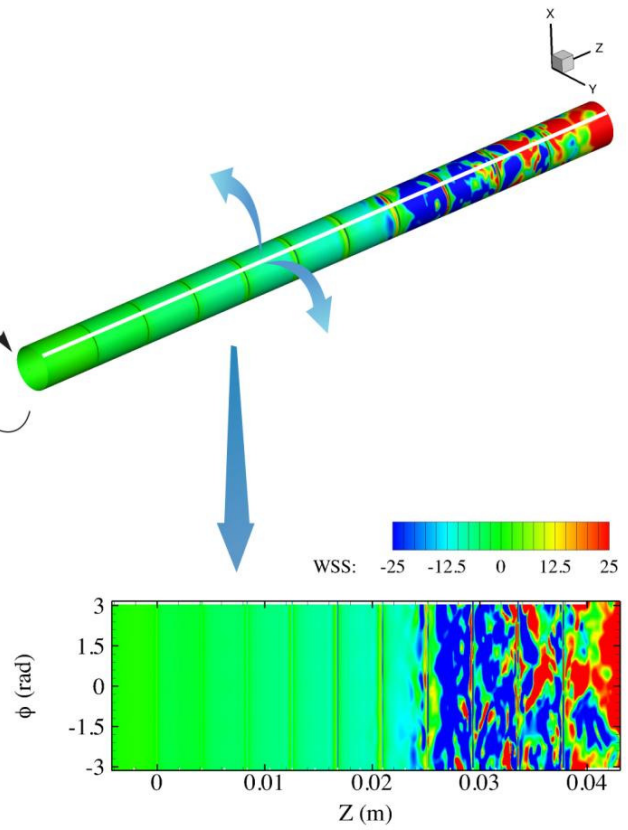

Fig. 2. The coronary artery is artificially cut open along the white line (top) and unwrapped into a 2-dimensional plane (bottom) to clearly display the contours of WSS in the azimuthally direction (ϕ).

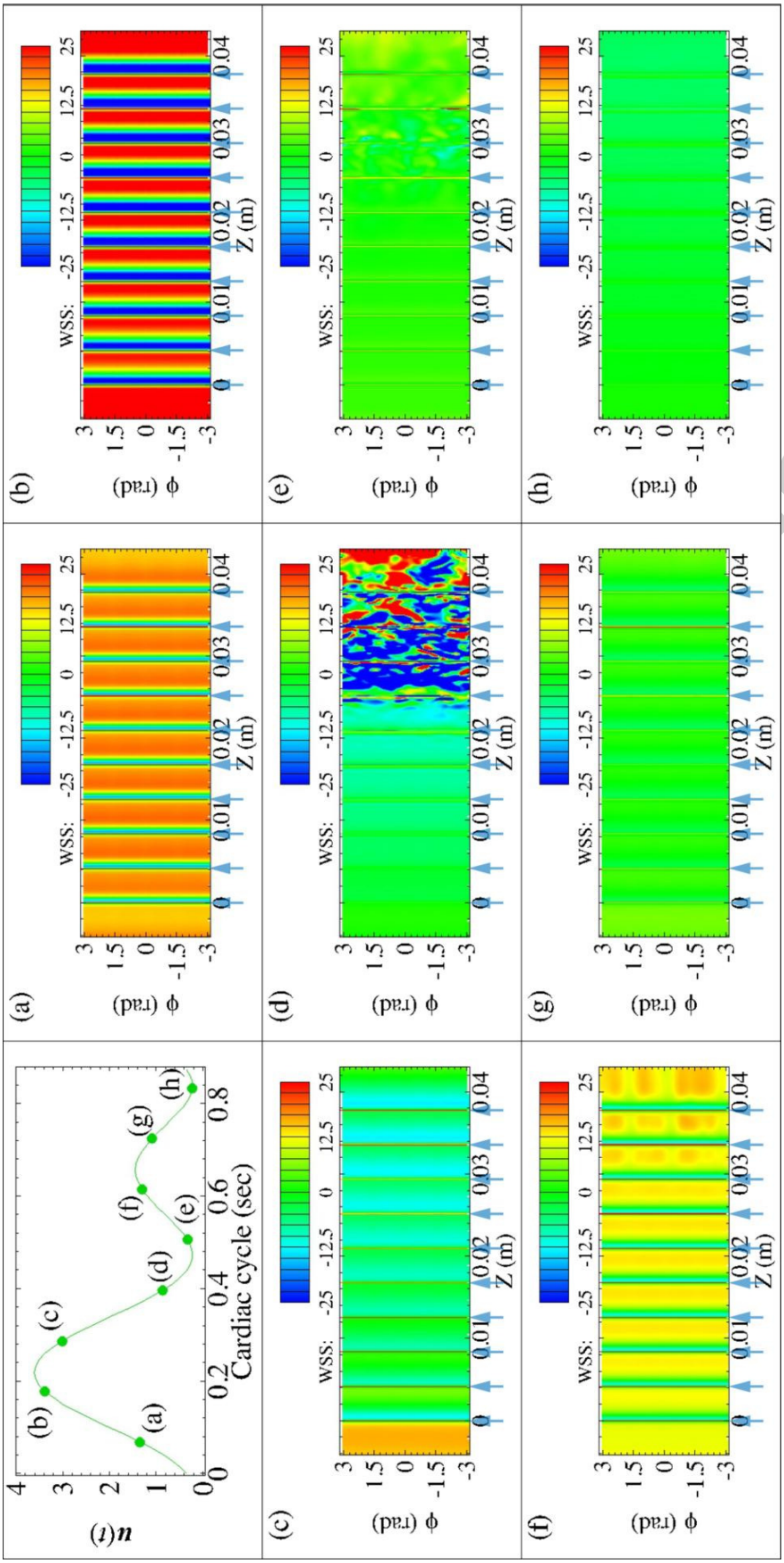

Fig. 3. Contours of WSS for square struts attached to the wall (MD = 0mm) on a 2-dimensional plane. Blue arrows indicate the centroid of each simplified coronary strut (ring).

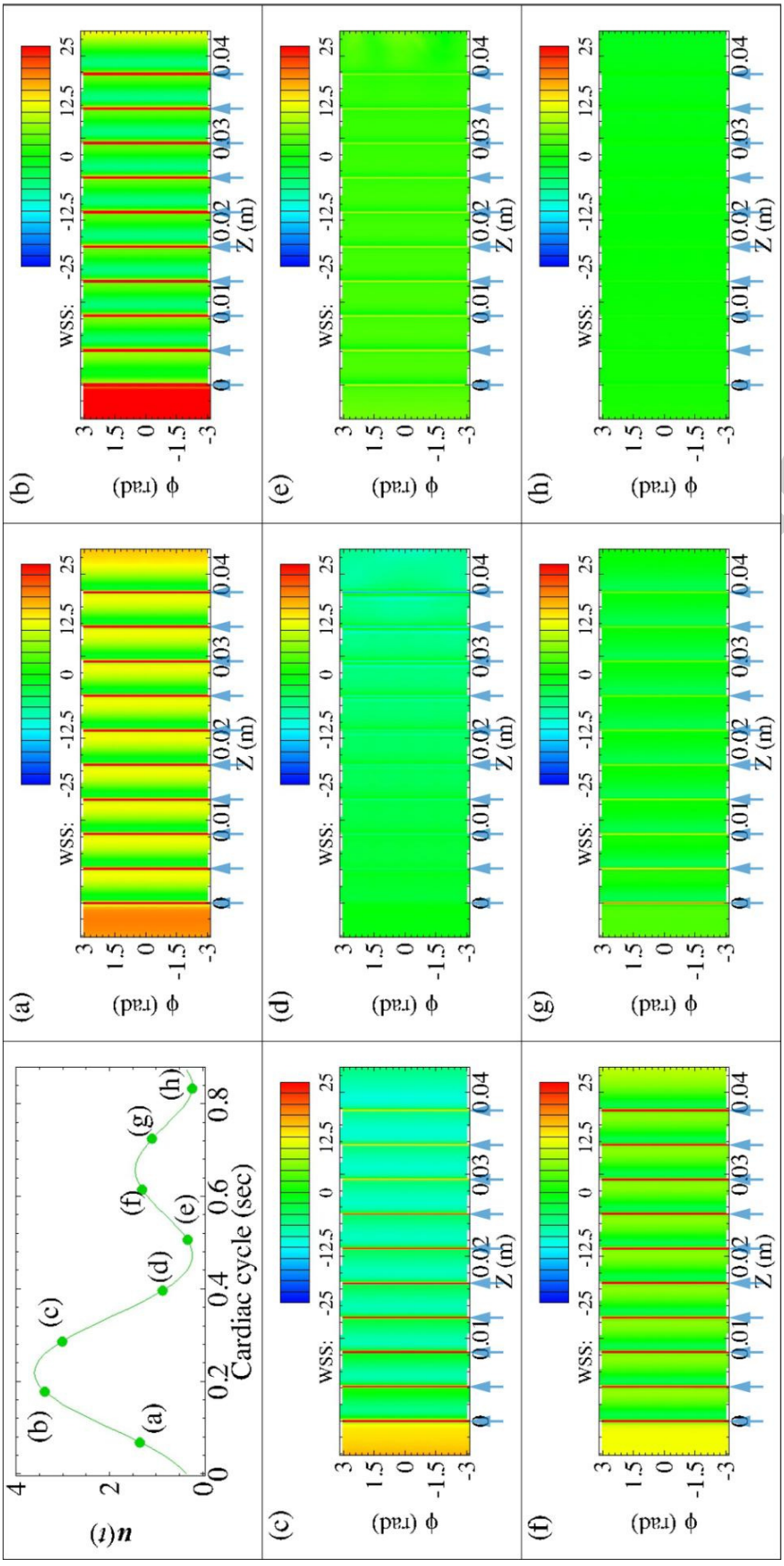

Fig. 4. Contours of WSS for malapposed square struts at MD = 0.06mm on a 2-dimensional plane. Blue arrows indicate the centroid of each simplified coronary strut (ring).

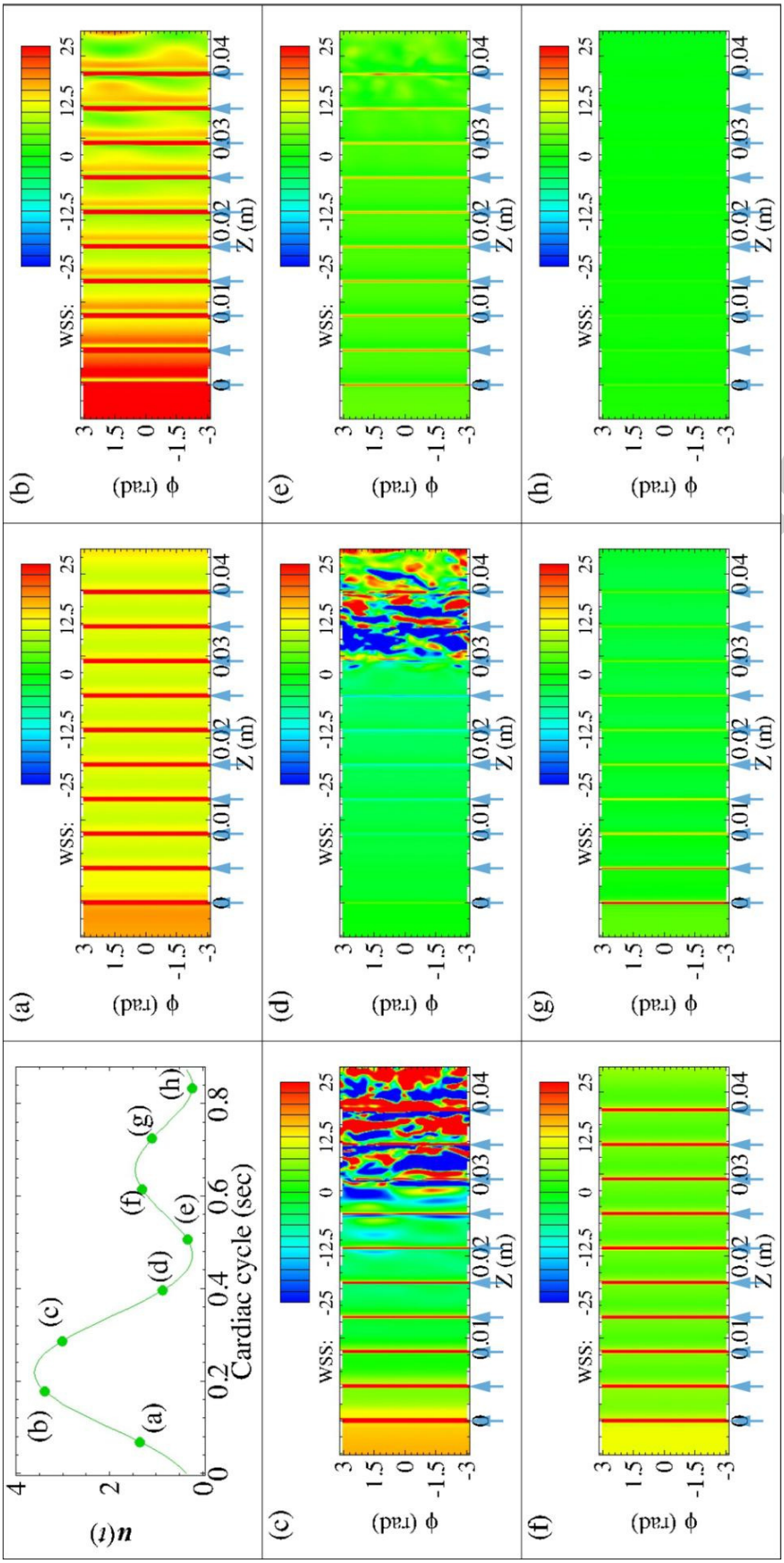

Fig. 5. Contours of WSS for malapposed square struts at MD = 0.12mm on a 2-dimensional plane. Blue arrows indicate the centroid of each simplified coronary strut (ring).

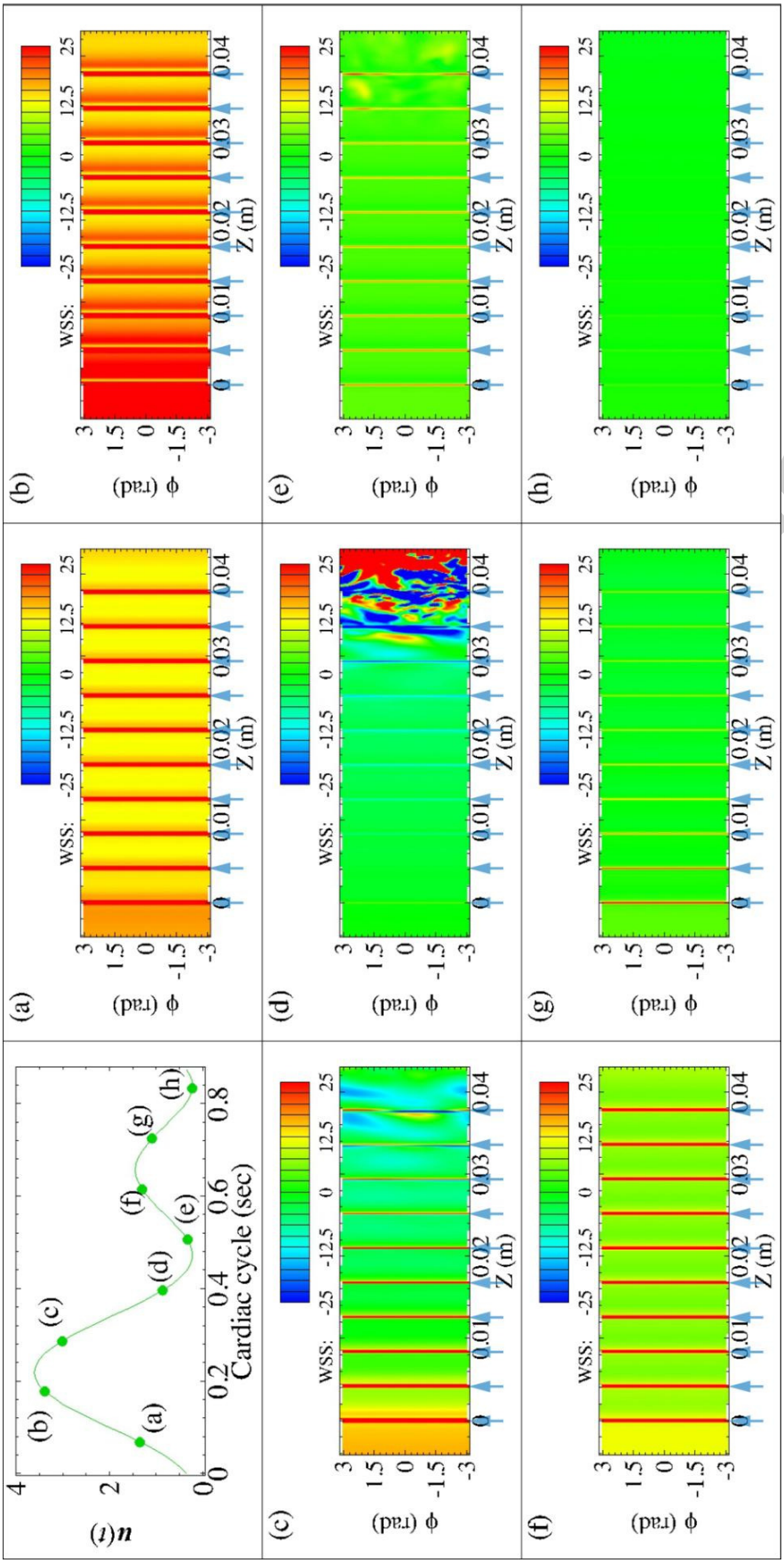

Fig. 6. Contours of WSS for malapposed circular struts at MD = 0.12mm on a 2-dimensional plane. Blue arrows indicate the centroid of each simplified coronary strut (ring).

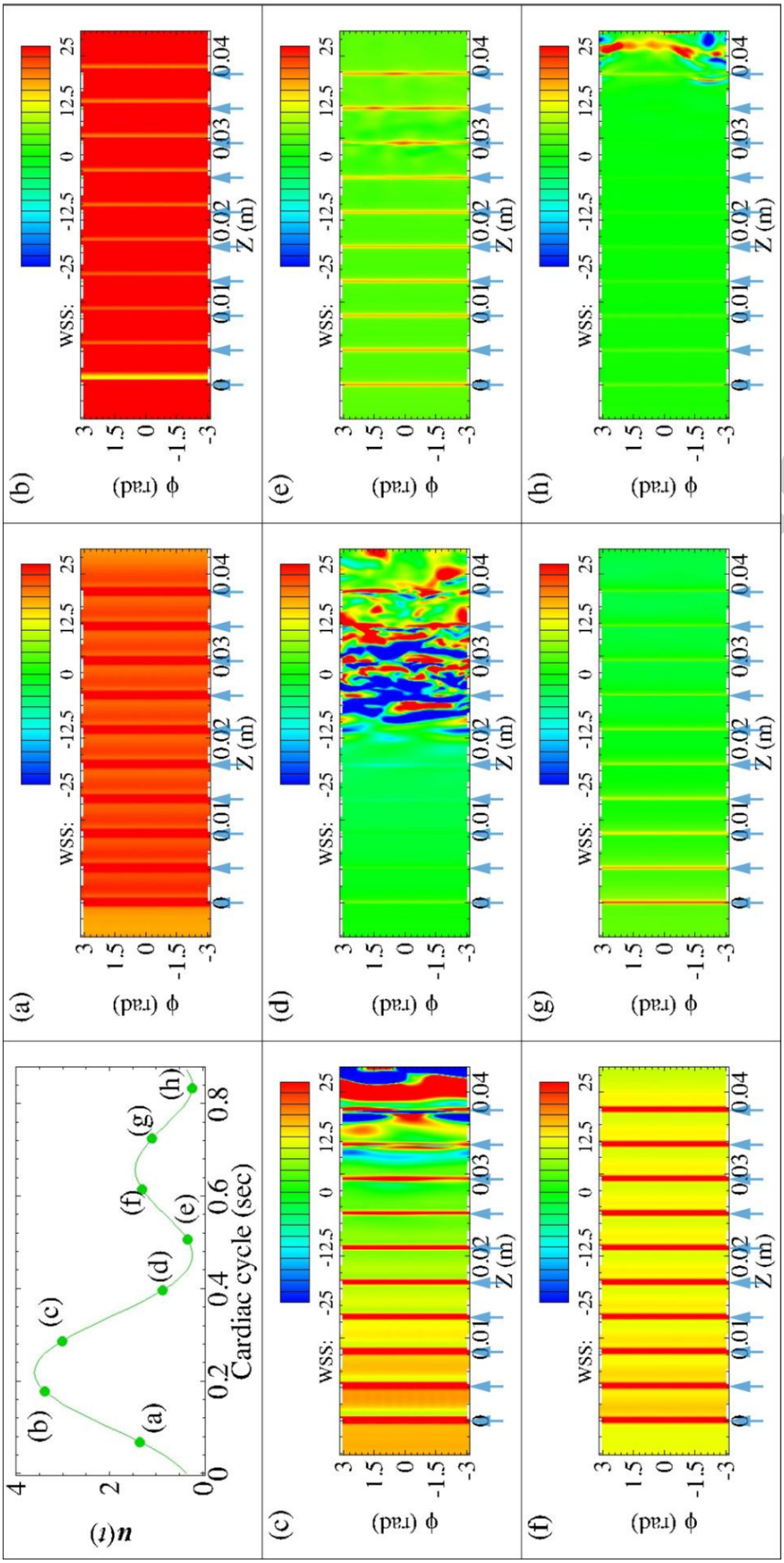

Fig. 7. Contours of WSS for malapposed circular struts at MD = 0.24mm on a 2-dimensional plane. Blue arrows indicate the centroid of each simplified coronary strut (ring).

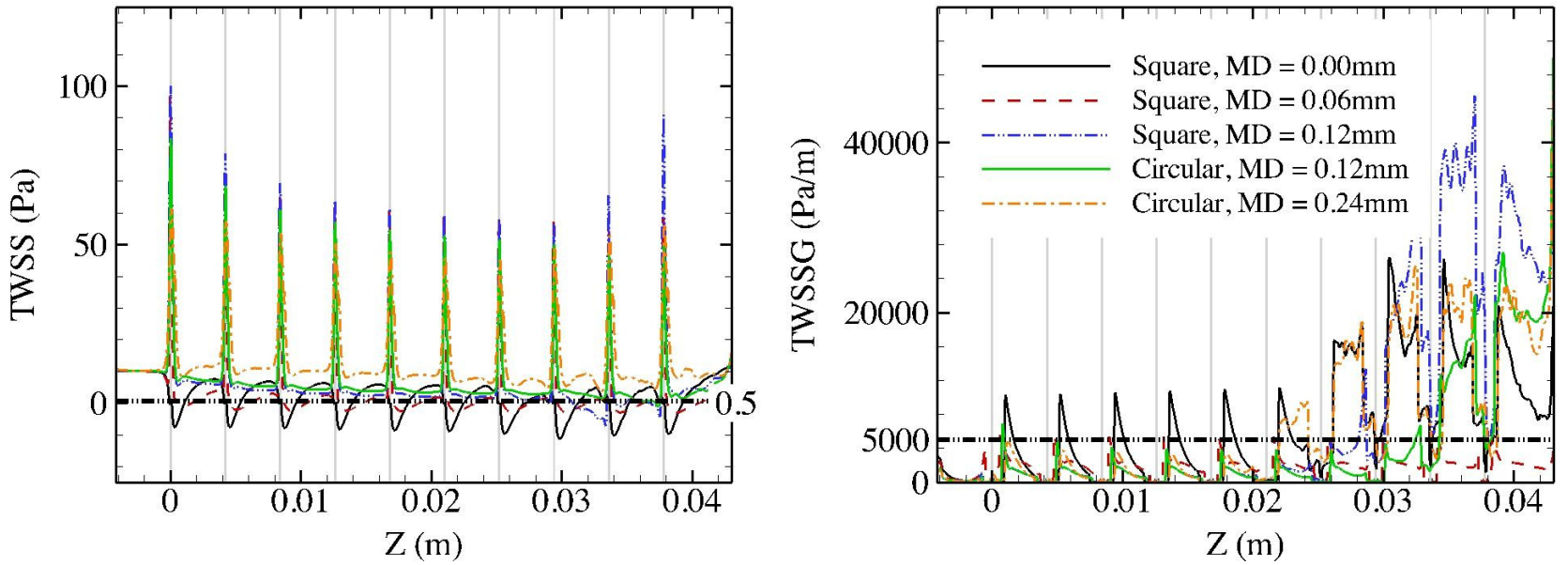

Fig. 8. Time-averaged wall shear stress (TWSS) and time-averaged wall shear stress gradient (TWSSG) for all cases considered. Both TWSS and TWSSG are spatially averaged in the azimuthal direction (ϕ). Grey shadows identify the location and the thickness of the simplified coronary stents (square/circular strut rings). The horizontal dash-dot-dot lines indicate the threshold values for TWSS and TWSSG.

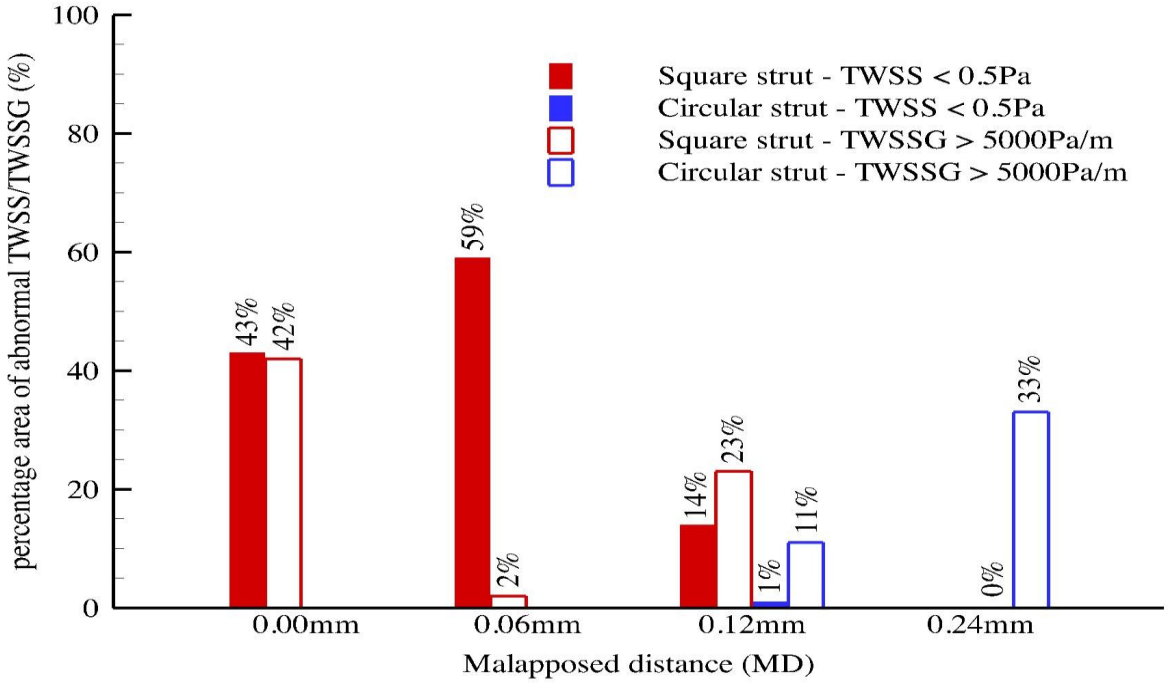

Fig. 9. Area of abnormal wall shear stress (WSS)/wall shear stress gradient (WSSG) relative to the stented area for various malapposition distance (MD). Lumen areas (mm^2) are affected by WSS < 0.5Pa and WSSG > 5000Pa/m.